

Variational dynamics of the sub-Ohmic spin-boson model on the basis of multiple Davydov D_1 states

Lu Wang,^{1,2} Lipeng Chen,¹ Nengji Zhou,³ and Yang Zhao^{1,*}

¹*Division of Materials Science, Nanyang Technological University, Singapore 639798, Singapore*

²*Department of Physics, Zhejiang University, Hangzhou 310027, China*

³*Department of Physics, Hangzhou Normal University, Hangzhou 310046, China*

(Dated: December 17, 2015)

Dynamics of the sub-Ohmic spin-boson model is investigated by employing a multitude of the Davydov D_1 trial states, also known as the multi- D_1 *Ansatz*. Accuracy in dynamics simulations is improved significantly over the single D_1 *Ansatz*, especially in the weak system-bath coupling regime. The reliability of the multi- D_1 *Ansatz* for various coupling strengths and initial conditions are also systematically examined, with results compared closely with those of the hierarchy equations of motion and the path integral Monte Carlo approaches. In addition, a coherent-incoherent phase crossover in the nonequilibrium dynamics is studied through the multi- D_1 *Ansatz*. The phase diagram is obtained with a critical point $s_c = 0.4$. For $s_c < s < 1$, the coherent-to-incoherent crossover occurs at a certain coupling strength, while the coherent state recurs at a much larger coupling strength. For $s < s_c$, only the coherent phase exists.

PACS numbers:

I. INTRODUCTION

It is of fundamental importance to study relaxation and coherence of open quantum systems attached to dissipative baths [1–4], a paradigm of which is the spin-boson model (SBM), describing a two-level system coupled with a bath of harmonic oscillators, as shown schematically in Fig. 1(a). The SBM has garnered attention due to its wide-ranging applications in a variety of physical situations, such as quantum computation [5–7], quantum phase transitions [8–12], spin dynamics [1, 3, 4] and electron transfer in biological molecules [13, 14]. The Hamiltonian of the SBM can be written as

$$\hat{H} = \frac{\epsilon}{2}\sigma_z - \frac{\Delta}{2}\sigma_x + \sum_l \omega_l b_l^\dagger b_l + \frac{\sigma_z}{2} \sum_l \lambda_l (b_l^\dagger + b_l), \quad (1)$$

where ϵ and Δ are the spin bias and the tunneling constant, respectively, σ_x and σ_z are Pauli matrices, b_l^\dagger (b_l) is the boson creation (annihilation) operator of the l th mode with frequency ω_l , and λ_l labels the spin-boson coupling strength associated with the l th mode. The environment and its coupling to the system are completely characterized by a spectral density function $J(\omega)$:

$$J(\omega) = \sum_l \lambda_l^2 \delta(\omega - \omega_l) = 2\alpha\omega_c^{1-s}\omega^s e^{-\omega/\omega_c} \quad (2)$$

where α is the dimensionless coupling strength, and ω_c denotes the cutoff frequency. The bosonic Ohmic bath is specified by $s = 1$, and $s < 1$ ($s > 1$) denotes the sub-Ohmic (super-Ohmic) bath. In the presence of an Ohmic bath, the SBM can be mapped onto the anisotropic

Kondo model using bosonization techniques [1], and there exists a Kosterlitz-Thouless-type phase transition that separates a non-degenerate delocalized phase from a doubly degenerate localized one, as well as a turnover from a coherent phase to an incoherent one. However, both the static and dynamic properties of the sub-Ohmic SBM are still under debate due to inherent difficulties in treating low-frequency bath modes.

Compared to the Ohmic case, the sub-Ohmic SBM is characterized by much pronounced coupling to the low-frequency bath modes, which makes it harder to describe the dynamics accurately as the low frequency modes generally lead to strongly non-Markovian dynamics and long-lasting bath memory effects. The sub-Ohmic SBM has been investigated by several sophisticated computational methods. The numerical renormalization group (NRG) approach developed by Wilson [15] seems to reveal a second order quantum phase transition for $0 < s < 1$ together with weakly damped coherent oscillations on short time scales even in the localized phase in the deep sub-Ohmic regime, i.e., $s \ll 1$. A continuous imaginary time cluster algorithm based on the quantum Monte Carlo (QMC) method has been recently proposed to study quantum phase transitions in the sub-Ohmic regime [10]. Contrary to the NRG results, the QMC critical exponents are found to be classical, mean-field like in the deep sub-Ohmic regime. An extension of the Silbey-Harris *Ansatz* [16] has been utilized to reveal a continuous transition with mean-field exponents for $0 < s < 0.5$ [17].

On the SBM dynamics, a consensus has yet to emerge on a basic physical picture. The phase diagram is shown schematically in Fig. 1(b). It is believed that for $s \leq 1$, with increasing coupling strength α , a dynamical coherent-incoherent crossover takes place first, followed by a delocalized-to-localized transition at a larger α , as revealed by the multilayer multiconfiguration time de-

*Electronic address: YZhao@ntu.edu.sg

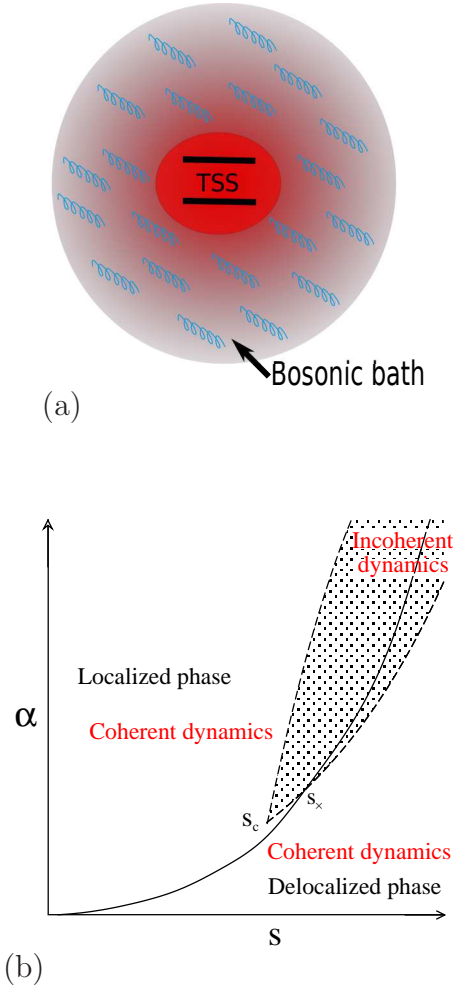


Figure 1: (a) Schematic of the SBM. (b) Sketch of the SBM phase diagram. The solid line which is the critical line of the localized-delocalized phase transition, partitions the domain into the delocalized (below) and the localized (above) phase. The two dashed lines are coherent-incoherent crossover lines. The lower crossover line intersects with the phase transition line at s_x and the two crossover lines meet at the critical point s_c . s_c separates the interval into two parts. For $s_c < s < 1$, the two dashed line separate the domain into three parts. The shaded area corresponds to the incoherent state and the other two are in the coherent state. For $s < s_c$, there is only coherent state.

pendent Hartree (ML-MCTDH) approach and the quantum master equation techniques [18–21]. As shown in Fig. 1(b), two transition lines meet at a critical exponent s_c , partitioning the plane into three parts for $s > s_c$. The shaded area corresponds to the incoherent phase, and the rest of domain belongs to the coherent phase. The solid line depicts the localized-delocalized phase transition and intersects with the coherent-incoherent transition line at an exponent point s_x larger than s_c . For an extended sub-Ohmic SBM including off-diagonal coupling, a similar phase diagram was found using an analysis of the response function [25]. Using the non-

interacting blip approximation (NIBA), $s_c = s_x = 0.5$ is obtained [22]. It is conjectured that for $s < s_c$, the coherent-incoherent crossover has larger α than the localized-delocalized phase transition [24]. Recently, real-time path integral Monte Carlo (PIMC) techniques show that below the critical point s_c , the nonequilibrium coherent dynamics can persist even under strong dissipation [22]. Reliable algorithms are needed to probe the dynamics accurately in the both weak and strong coupling strength regimes.

The SBM is analogous to the one-exciton, two-site version of the Holstein molecular crystal model [26], and it is well known that the Davydov *Ansatz* and its variants [27–30] are successful trial states in treating both static and dynamic properties of the Holstein polaron. In addition, the single Davydov D_1 *Ansatz* has been applied to probe the dynamics of the sub-Ohmic SBM [31], and it is shown that, counterintuitively, even in the very strong coupling regime, quantum coherence features manage to survive under the polarized bath initial condition, in agreement with the PIMC results [22]. Very recently, a multitude of Davydov D_1 *Ansatz* (the multi- D_1 *Ansatz*) has been successfully constructed to study the ground-state properties of the sub-Ohmic SBM with simultaneous diagonal and off-diagonal coupling. Much more accurate results near the quantum phase transition point, in agreement with those from the methods of density matrix renormalization group and exact diagonalization, have been obtained by the multi- D_1 *Ansatz* [32, 33] than those by the single D_1 *Ansatz*. However, how the multi- D_1 *Ansatz* fares with the dynamics of the SBM with an arbitrary initial state remains an issue to be addressed.

In this paper, a time-dependent version of the multi- D_1 *Ansatz* [32] is adopted to formulate an accurate description of dynamic properties of the sub-Ohmic SBM with various system-bath coupling strengths, based on the Dirac-Frenkel time-dependent variational principle. The reliability and robustness of the *Ansatz* are systematically probed, in comparison with the hierarchy equations of motion (HEOM) and the PIMC approaches. The rest of the paper is organized as follows. The multi- D_1 *Ansatz* and relevant physical quantities for the SBM are introduced in Sec. II. In Sec. III, we present numerical results, examine the discretization parameters for convergent results and show the superiority of the multi- D_1 *Ansatz*. In Sec. IV, the reliability of the multi- D_1 *Ansatz* are checked by comparing results from our method to those from the HEOM and PIMC approaches. Furthermore, The dynamical coherent-incoherent crossover is investigated through the multi- D_1 *Ansatz*. Finally, Conclusions are drawn in Sec. V.

II. METHODOLOGY

A. Dirac-Frenkel Variation

The multi-D₁ *Ansatz* is an improved trial wave function as compared to the single D₁ *Ansatz* [31]. The time-dependent version of the multi-D₁ *Ansatz* can be written as

$$\begin{aligned} |D(t)\rangle &= |+\rangle \sum_{n=1}^M A_n(t) \exp \left(\sum_l f_{nl}(t) b_l^\dagger - \text{H.c.} \right) |0\rangle_{\text{ph}} \\ &+ |-\rangle \sum_{n=1}^M B_n(t) \exp \left(\sum_l g_{nl}(t) b_l^\dagger - \text{H.c.} \right) |0\rangle_{\text{ph}}, \end{aligned} \quad (3)$$

where H.c. denotes the Hermitian conjugate, $|+\rangle$ ($|-\rangle$) stands for the spin-up (spin-down) state, and $|0\rangle_{\text{ph}}$ is the vacuum state of the boson bath. $A_n(t)$ and $B_n(t)$ are variational parameters representing the amplitudes in states $|+\rangle$ and $|-\rangle$, respectively, and $f_{nl}(t)$ and $g_{nl}(t)$ are the corresponding phonon displacements, where n and l denote the n th coherent state and the l th effective bath mode, respectively. M is the multiplicity, and the multi-D₁ *Ansatz* is reduced to the Davydov D₁ *Ansatz* when $M = 1$.

Adopting the Lagrangian formalism of the Dirac-Frenkel time-dependent variational principle, one can derive equations of motion (EOM) for the variational parameters,

$$\frac{d}{dt} \left(\frac{\partial L}{\partial \dot{u}_n^*} \right) - \frac{\partial L}{\partial u_n^*} = 0, \quad (4)$$

where u_n^* denotes the complex conjugate of the variational parameters u_n , which can be A_n , B_n , f_{nl} , or g_{nl} . The readers are referred to Appendix A for the detailed derivation of EOM for the variational parameters. The Lagrangian L in Eq. (4) associated with the trial state $|D(t)\rangle$ is defined as

$$\begin{aligned} L &= \frac{i}{2} \left\langle D(t) \left| \frac{\partial}{\partial t} \right| D(t) \right\rangle - \frac{i}{2} \left\langle D(t) \left| \frac{\partial}{\partial t} \right| D(t) \right\rangle \\ &- \left\langle D(t) \left| \hat{H} \right| D(t) \right\rangle. \end{aligned} \quad (5)$$

B. Spectral Density Discretization

The bath is completely characterized by the spectral density function through the parameters λ_l in Eq. (1), labeling the coupling strength of the spin to the l th bath mode with frequency ω_l . Using a discretization procedure, λ_l can be obtained from the spectral density function as shown in Eq. (2). There are various discretization methods to achieve λ_l . The simplest procedure is the linear discretization [31]. One divides the frequency domain

$[0, \omega_{\text{max}}]$ into N_b equal intervals $\Delta\omega$, in which N_b is the number of effective bath modes and $\omega_{\text{max}} = 4\omega_c$ is the upper bound of the frequency. The lower bound of the procedure is $\omega_{\text{min}} = \Delta\omega = \omega_{\text{max}}/N_b$ and the l th frequency is $\omega_l = l\Delta\omega$. The parameter λ_l^2 can be expressed as

$$\lambda_l^2 = J(\omega_l) \Delta\omega, \quad (6)$$

by calculating the integral of the spectral density Eq. (2) over ω ,

$$\sum_{l=1}^{N_b} \lambda_l^2 = \int_0^\infty d\omega J(\omega) \approx \sum_{l=1}^{N_b} J(\omega_l) \Delta\omega. \quad (7)$$

In the linear discretization procedure, the number of modes N_b can effect the dynamics in two aspects. Firstly, the Poincaré recurrence time $T_p = 2\pi/\Delta\omega$ is determined by ω_{min} . If the number of modes is not large enough, artificial recurrence occurs in the time period of interest. Secondly, in the sub-Ohmic regime, the dynamics of the observables may be sensitive to the low frequency modes. The number of modes required may vary for different initial bath conditions, such as the factorized and polarized initial baths (see details in Sec. III). Under the factorized bath initial condition, the dynamics is insensitive to the number of phonon modes. However, the influence of N_b on the dynamics with the polarized bath is considerable. For the linear discretization, a proper $\Delta\omega$ is needed to guarantee that the recurrence time is longer than time interval we are interested in and sufficiently low frequencies are sampled. Thus, the simulation is reliable only when numerous modes are sampled. Over ten thousand modes are required in order to obtain sufficiently low ω_{min} in the linear discretization scheme. Therefore, this discretization method requires an enormous number of EOM to be solved, leading to CPU time and memory constraints, as well as numerical instabilities.

The sub-Ohmic SBM, characterized by the effect of coupling to the low frequency bath modes, has long-lasting bath memory effects. It is possible to employ another discretization method to circumvent the disadvantage of linear discretization and reach a compromise between accuracy and computational efficiency by focusing on the low frequency domain. A method termed the logarithmic discretization is extensively employed by the NRG techniques to probe ground-state properties [15]. One divides the frequency domain $[0, \omega_{\text{max}}]$ into N_b intervals, $[\Lambda^{-(l+1)}, \Lambda^{-l}] \omega_{\text{max}}$ ($l = 0, 1, 2, \dots, N_b - 1$). The parameters λ_l and ω_l in Eq. (1) can then be obtained as

$$\lambda_l^2 = \int_{\Lambda^{-(l+1)} \omega_{\text{max}}}^{\Lambda^{-l} \omega_{\text{max}}} dx J(x), \quad (8)$$

and

$$\omega_l = \lambda_l^{-2} \int_{\Lambda^{-(l+1)} \omega_{\text{max}}}^{\Lambda^{-l} \omega_{\text{max}}} dx J(x) x. \quad (9)$$

The logarithmic discretization can easily characterize the spectral density function in the low frequency domain. The relatively large discretization parameters such as $\Lambda = 2$ or 1.5 are usually employed in the NRG method, because only the ground state is of interest. Nevertheless for the dynamics, the excited states are important as well. Smaller Λ should be used, to sample sufficiently low frequencies and take into account the effect of the high frequencies. For the small Λ , the logarithmic discretization is an approximation to the linear discretization. The relative weight between different λ_l is distorted by the partition of the integral. The distortion can only be improved when $\Lambda \rightarrow 1$. It is difficult to estimate the Poincaré recurrence time under the logarithmic discretization. The recurrence occurs even when ω_{\min} is sufficiently small for a large Λ . In accordance to the previous discussion, we will adopt a logarithmic discretization due to its computational efficiency. Convergence of the results must be carefully analyzed in each case.

C. Observables

From Eq. (3), the norm of the trial wave function can be calculated as

$$\begin{aligned} \mathcal{N}(t) &= \langle D(t) | D(t) \rangle \\ &= \sum_{n,u=1}^M [A_n^* A_u R(f_n^*, f_u) + B_n^* B_u R(g_n^*, g_u)] \end{aligned} \quad (10)$$

where $R(f_n^*, g_u) = \langle f_n | g_u \rangle$ is the Debye-Waller factor defined as

$$R(f_n^*, g_u) \equiv \exp \left[\sum_l \left(f_{nl}^* g_{ul} - \frac{1}{2} |f_{nl}|^2 - \frac{1}{2} |g_{ul}|^2 \right) \right], \quad (11)$$

with the coherent state

$$|g_m\rangle = \exp \left[\sum_l g_{ml}(t) b_l^\dagger - \text{H.c.} \right] |0\rangle_{\text{ph}}. \quad (12)$$

It is well known that, the norm of the wave function $\mathcal{N}(t)$ should be unity at any time t , a fact that can be used to test the accuracy of the variational dynamics. In the SBM, physical observables of interest are,

$$P_i(t) \equiv \langle \sigma_i \rangle = \langle D(t) | \sigma_i | D(t) \rangle, \quad i = x, y, z. \quad (13)$$

Here, $P_x(t)$ and $P_y(t)$ represent the real and imaginary part of the coherence between the spin-up and spin-down states, respectively, and $P_z(t)$ describes the population difference. By substituting the trial wave function of Eq. (3) into Eq. (13), these quantities can be easily der-

rived as

$$\begin{aligned} P_x(t) &= \sum_{n,u=1}^M [A_n^* B_u R(f_n^*, g_u) + B_n^* A_u R(g_n^*, f_u)], \\ P_y(t) &= -i \sum_{n,u=1}^M [A_n^* B_u R(f_n^*, g_u) - B_n^* A_u R(g_n^*, f_u)], \\ P_z(t) &= \sum_{n,u=1}^M [A_n^* A_u R(f_n^*, f_u) - B_n^* B_u R(g_n^*, g_u)]. \end{aligned} \quad (14)$$

To investigate the entanglement between the spin and the bath, we introduce the von Neumann entropy [34, 35],

$$S_{\text{v-N}} = -\omega_+ \ln \omega_+ - \omega_- \ln \omega_-, \quad (15)$$

where

$$\omega_{\pm} = (1 \pm \sqrt{P_x^2 + P_y^2 + P_z^2})/2 \quad (16)$$

are the eigenvalues of the reduced density matrix obtained by tracing the density matrix over the bath degrees of freedom.

III. NUMERICAL RESULTS

The dynamical behavior of the sub-Ohmic SBM is sensitive to the bath initial conditions [22, 24, 31]. Two initial conditions are often considered for the phonon displacements: one is the factorized initial condition corresponding to the phonon vacuum state with $f_{nl}(0) = g_{nl}(0) = 0$, and the other is the polarized initial condition corresponding to a displaced-oscillator state with $f_{nl}(0) = g_{nl}(0) = -\lambda_l/2\omega_l$ [31]. The spin is assumed to initially occupy the up state $|+\rangle$, i.e., $A_1(0) = 1$, $B_1(0) = 0$ and $A_n(0) = B_n(0) = 0$ ($n \neq 1$). In order to avoid singularities, uniformly distributed noise within $[-\varepsilon, \varepsilon]$ is added to the initial spin amplitudes ($\varepsilon = 10^{-4}$) and phonon displacements ($\varepsilon = 10^{-2}$). Results have been averaged for a sufficiently large sampling size such that the errors induced by the noise are negligible.

In some previous work, such as Ref. [24], “weak coupling” usually denotes values of α that fall below the localized-delocalized transition point α_c . In this work, however, we focus on the dynamics of the sub-Ohmic SBM, and we use “weak coupling” to refer to the parameter space of small α in which the observables, such as P_z , behave as those in an underdamped oscillator.

A. Dynamical behavior of the sub-Ohmic SBM

The bosonic bath acts as a damping mechanism and the coupling strength α parameterizes the strength of the damping. Probing the properties of the dynamical observables with varying α offers insights into the quantum system in a dissipative environment. In this subsection,

we investigate the time evolution of the population difference $P_z(t)$, the coherence between $|+\rangle$ and $|-\rangle$ $P_x(t)$, and the von Neumann entropy $S_{v-N}(t)$ by using the multi-D₁ *Ansatz*. In the SBM, the two energy levels $|+\rangle$ and $|-\rangle$ can be used to describe the donor and acceptor states in electron transfer, and then $P_z(t)$ is the population difference. $P_x(t)$ is related to the off-diagonal part of the reduced density matrix and describes the tunneling between the two energy levels. $S_{v-N}(t)$ characterizes the information flow between the system and the bath.

In Fig. 2(a), the population difference $P_z(t)$ is plotted for various coupling strengths α with the factorized initial bath. All coupling strengths in the simulations are above the localized-delocalized phase transition point $\alpha_c = 0.022$, thus the equilibrium value of $P_z(t)$, P_{eq} , does not vanish. With increasing α , P_{eq} approaches 1. In the weak coupling regime of $\alpha \in [0.03, 0.07]$, $P_z(t)$ oscillates and its amplitude decays with time, as in a damped oscillator. With increasing α in the range of $[0.03, 0.07]$, the bath becomes more dissipative and the amplitude of $P_z(t)$ decreases, while the frequency of the oscillation almost does not change. In the strong coupling regime above $\alpha = 0.07$, the amplitude of oscillation is suppressed severely by damping. $P_z(t)$ quickly decays to P_{eq} then holds a steady-state value for long times, similar to that in overdamped dynamics often represented as an exponential decay. As displayed in Fig. 2(a), for $\alpha = 0.1$, however, a lobe highlighted by the dashed line exists below P_{eq} , which deviates from the overdamped dynamics. For larger α , the lobe still exists and is not marked by the small amplitude. In addition, $P_z(t)$ reaches its minimum faster with increasing α implying the oscillation frequency turns higher. The higher frequency makes coherence possible before being suppressed by the decay. The phenomenon of coherent dynamics surviving under arbitrary large coupling for $s < 1/2$, is first uncovered by the PIMC method using the dynamics of $P_z(t)$ with $s = 0.25$ and the polarized initial bath as an example [22]. In the Sec. IV B, we will discuss in detail such sustained coherence.

To probe the dynamics of the coherence between $|+\rangle$ and $|-\rangle$, $P_x(t)$ is calculated for $s = 0.25$ with the factorized initial bath. Initially, $P_x(t)$ increases rapidly with time for all coupling strengths with a larger slope for stronger coupling. A larger α leads to more rapidly evolving system dynamics, thus the slope of $P_x(t)$ for the short times increases with increasing α . For long times, the dynamical behaviors vary depending on the coupling strength. For strong coupling, $\alpha > 0.07$, $P_x(t)$ first reaches its maximum before leveling off gradually. The stronger the coupling is, the faster $P_x(t)$ reaches its maximum. And the maximum of $P_x(t)$ is depressed by increasing α . For ultra-strong coupling $\alpha = 0.3$, after a decrease from its maximum, $P_x(t)$ holds a steady value. Strong coupling shortens the oscillation time scale of $P_x(t)$, a phenomenon also observed in the dynamics of $P_z(t)$. The coherence between the two states is destructed under the impact of the bath for long times. For

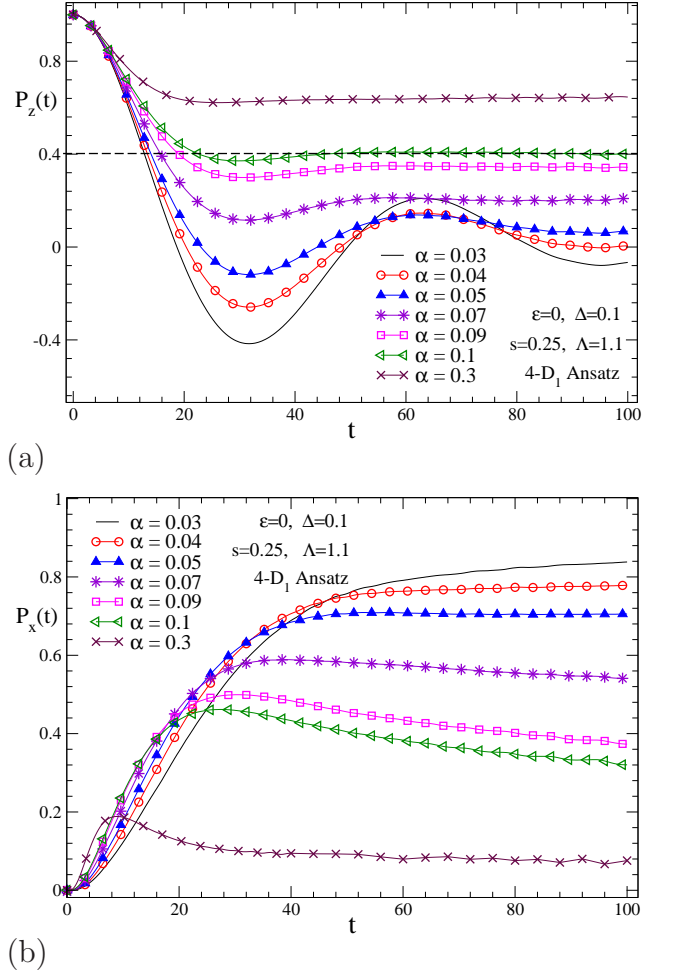


Figure 2: (a) The time evolution of the population difference $P_z(t)$, and (b) the spin coherence $P_x(t)$ under a factorized bath initial condition are shown for various coupling $\alpha = 0.03, 0.04, 0.05, 0.07, 0.1$ and 0.3 . Other Parameters used are $s = 0.25$, $\Delta/\omega_c = 0.1$, $\epsilon = 0$, $M = 4$ and $N_b = 180$. The dashed line plotted on the steady-state value of $P_z(t)$ for $\alpha = 0.1$, shows the existence of the weak oscillations for strong coupling.

weak coupling, $\alpha \in [0.03, 0.07]$, after a transient stage, P_x reaches a saturated value. The dynamics for longer times is unknown and will be probed in further investigations.

To characterize the entanglement between the spin and bath, the von Neumann entropy $S_{v-N}(t)$ is plotted in Fig. 3(a) for the factorized initial bath. It is found that $S_{v-N}(t)$ is quickly damped to a steady-state value, especially for the coupling strength α above 0.05 . Though the steady values of $P_z(t)$ and $P_x(t)$ decrease monotonically with the increasing coupling strength, those of $S_{v-N}(t)$ are nonmonotonic function of α and the maximum steady-state value occurs at $\alpha \approx 0.09$, slightly different from $\alpha \approx 0.07$ as obtained by the single D₁ *Ansatz* [31]. And our results show that, for long times, $S_{v-N}(t)$ reaches steady-state values, in disagreement with the

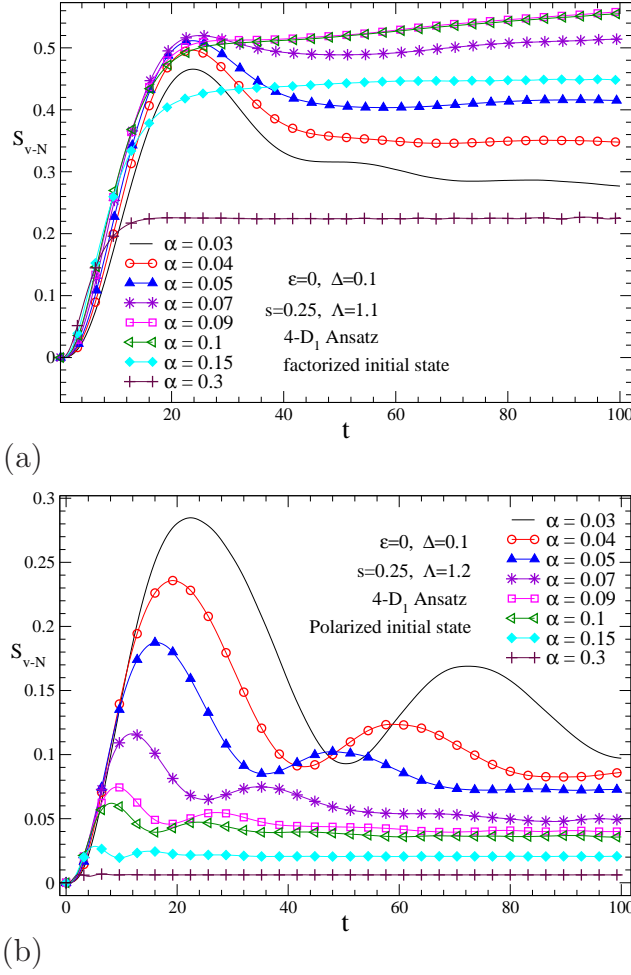


Figure 3: The time evolution of the von Neumann entropy S_{v-N} under (a) the factorized bath initial condition, and (b) the polarized bath initial condition for $\alpha = 0.03, 0.04, 0.05, 0.07, 0.09, 0.1, 0.15$ and 0.3 . Other parameters are $s = 0.25$, $\Delta/\omega_c = 0.1$, $\epsilon = 0$ and $M = 4$.

conclusion in Ref. [22] that it will tend to zero in the strong coupling regime. To clarify this contradiction, simulations are performed with the same polarized initial bath as in Ref. [22] for $S_{v-N}(t)$, and results are shown in Fig. 3(b). It is found that the entropy oscillates even when the coupling is very strong and such a dynamical behavior is consistent with the coherent $P_z(t)$ found in the very strong coupling regime (see Fig. 10). For the long times and with strong coupling, $S_{v-N}(t)$ also retains a steady-state value which decreases monotonically with increasing α . Thus, it is our guess that the time interval studied in Ref. [22] may be too short to observe stable values of $S_{v-N}(t)$. For the sub-Ohmic SBM, $S_{v-N}(t)$ may approach zero very slowly, and the asymptotic behavior is beyond the reach of our approach as employed in this work.

B. Discretization parameters

If not carefully carried out, simulation of the SBM dynamics can be artificially influenced by parameters that include the logarithmic discretization parameter Λ and the frequency lower bound ω_{\min} . In this subsection, a careful convergence test is performed for Λ and ω_{\min} .

To check the dependence of the computation convergence on Λ , $P_z(t)$ is simulated for $\alpha = 0.03$, $\omega_{\min} \approx 10^{-7}$, $\Lambda = 2, 1.5, 1.2$ and 1.1 , as shown in Fig. 4. For short times, dynamics computed with different values of Λ are nearly identical, but distinguishable deviations can be found at longer times. For the curves with $\Lambda = 2$ and 1.5 , there exist high frequency oscillations which are an artifact as the system cannot afford such high-energy oscillations. While for the curves with $\Lambda = 1.2$ and 1.1 , the oscillations disappear and the difference between the two curves is negligibly small, which shows that the results are convergent for these values of Λ . As mentioned in Sec. II B, the Poincaré recurrence time T_p is difficult to estimate using the logarithmic procedure. Shown by our simulations, with nearly identical ω_{\min} , the recurrence occurs for larger Λ , i.e., $\Lambda = 2$ and 1.5 . We conclude that T_p is also dependent on Λ using the logarithmic discretization. In order to obtain reliable results, a smaller Λ should be chosen until the artificial oscillations disappear.

To probe the proper frequency lower bound ω_{\min} , we perform simulations for $P_z(t)$ for various numbers of modes N_b with $\alpha = 0.03$ and both the factorized and polarized initial baths, and results are shown in Fig. 5. We choose $\omega_{\min} \approx 10^{-3}, 10^{-4}, 10^{-5}, 10^{-6}, 10^{-7}$ and 10^{-8} , which corresponds to $N_b = 85, 110, 160, 180, 210$ and 231 , respectively, to perform the simulations with $\Lambda = 1.1$. In Fig. 5(a), the results with the factorized initial bath are plotted. All curves are found to coincide with each other, demonstrating that with the factorized initial bath, the dynamics is insensitive to the low frequency modes. However, with the polarized initial bath, the results vary with the number of modes N_b drastically, as shown in Fig. 5(b). Convergence is reached only after the frequency lower bound is reduced to $\omega_{\min} \approx 10^{-7}$. The dependence of $P_z(t)$ on ω_{\min} can be explained by a dynamical asymmetry, i.e., a time-dependent bias, coming from the coupling term $\sigma_z/2 \sum_l \lambda_l (b_l^\dagger + b_l)$ in the Hamiltonian of Eq. (1). As revealed by Ref. [24], the system first relaxes to a quasi-equilibrium state as determined by the dynamical asymmetry, and then the asymmetry decays very slowly. The average position of $P_z(t)$ is dominated by the low-frequency phonons. Thus, the ω_{\min} must be small enough to make the contribution of the modes below ω_{\min} to the coupling term negligibly small. Our results show that the frequency lower bound ω_{\min} yielding convergence with the factorized bath may be different from that with the polarized bath even for the same coupling strength. The convergence test for the number of modes must be performed for each type of initial bath conditions.

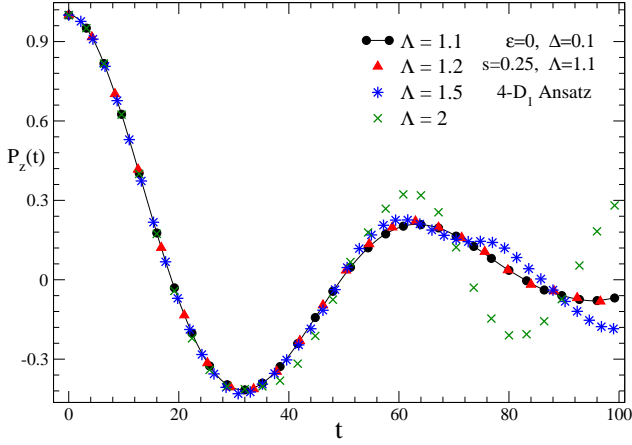


Figure 4: The population difference $P_z(t)$ obtained by the multi- D_1 *Ansatz* with discretization parameters $\Lambda = 1.1, 1.2, 1.5$ and 2 are compared. The factorized bath initial condition is employed. Other parameters are $s = 0.25$, $\alpha = 0.03$, $\Delta/\omega_c = 0.1$ and $\epsilon = 0$.

C. Accuracy of the multi- D_1 *Ansatz*

The multi- D_1 *Ansatz* is an extension of the Davydov *Ansatz*. It is known that the Davydov single D_1 *Ansatz* performs well in the strong and intermediate coupling regimes [3]. It may be less accurate in the weak coupling regime. In this subsection, we will compare the results from the multi- D_1 *Ansatz* with those from the single D_1 *Ansatz* in the both weak and strong coupling regimes.

Figure 6 shows the time evolution of the population difference $P_z(t)$ calculated by the single D_1 and the multi- D_1 *Ansätze* under the factorized initial condition. In the weak coupling regime (such as $\alpha = 0.03$), both the amplitudes and oscillation frequencies of $P_z(t)$ from the multi- D_1 *Ansatz* deviate significantly from those calculated by the single D_1 *Ansatz*. This is because the phonon wave function exhibits plane-wave like behavior in the weak coupling regime, thus more phonon coherent states are needed to capture the accurate dynamics. For strong coupling cases of $\alpha = 0.1$ and 0.3 , the single D_1 *Ansatz* still has room for improvements, though the difference between the two curves is very small. At $s = 0.25$, the single D_1 *Ansatz* only displays incoherent dynamics when $\alpha \geq 0.1$. While according to Ref. [22], for the SBM in the deep sub-Ohmic regime, the coherence survives for any large coupling strength. These results indicate that the multi- D_1 *Ansatz*, as an improved trial wave function, can treat both weak and strong coupling in a unified manner and captures more accurately dynamic properties.

To check the validity of the trial *Ansatz*, we define the relative deviation $\sigma(M, t)$ for the trial state $|D(M, t)\rangle$,

$$\sigma(M, t) = \sqrt{\langle \delta(M, t) | \delta(M, t) \rangle} / \bar{E}_{\text{bath}}, \quad (17)$$

where $|\delta(M, t)\rangle$ is the deviation vector quantifying how

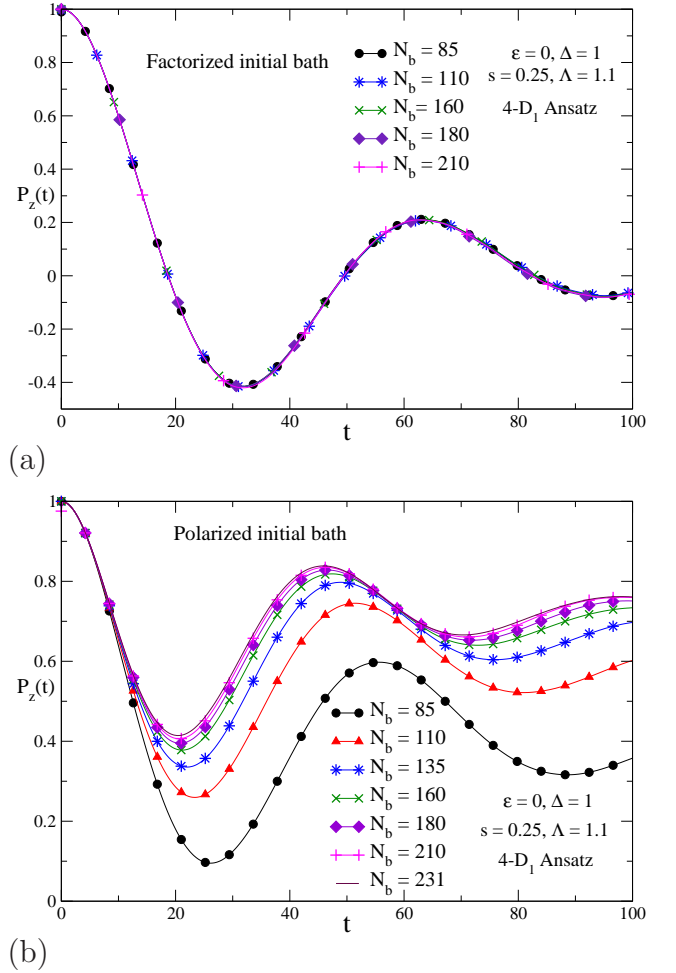


Figure 5: The population difference $P_z(t)$ obtained by the multi- D_1 *Ansatz* with various mode numbers N_b are compared. (a) The factorized bath initial condition, and (b) the polarized bath initial condition are employed. The discretization parameter $\Lambda = 1.1$. Other parameters are $s = 0.25$, $\alpha = 0.03$, $\Delta/\omega_c = 0.1$ and $\epsilon = 0$.

faithfully $|D(M, t)\rangle$ follows the Schrödinger equation,

$$|\delta(M, t)\rangle = \left(i \frac{\partial}{\partial t} - \hat{H} \right) |D(M, t)\rangle, \quad (18)$$

and \bar{E}_{bath} is the average energy of the bath within the simulation time. Generally speaking, the smaller $\sigma(M, t)$ as a function of the multiplicity M , the more accurate the trial state $|D(M, t)\rangle$ is. Shown in Fig. 7 for four coupling strengths, $\alpha = 0.03, 0.04, 0.05$ and 0.1 , are the maximum values of $\sigma(M, t)$, σ_{max} , during the simulation time period. For $M = 1$, σ_{max} for $\alpha = 0.1$ is much smaller than those for the weak coupling cases of $\alpha = 0.03, 0.04$ and 0.05 , which shows the single D_1 *Ansatz* is more accurate for strong coupling. Comparatively, σ_{max} for the multi- D_1 *Ansatz*, are much smaller than those for the single D_1 *Ansatz*. To probe the asymptotic value of

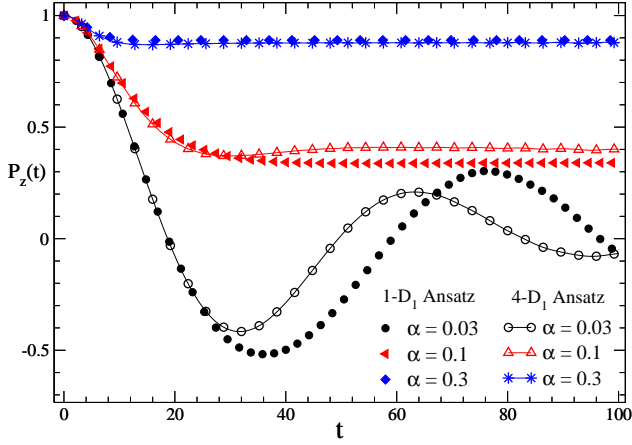


Figure 6: Results of population difference $P_z(t)$ under the factorized bath initial condition from the single D_1 Ansatz ($M = 1$) and multi- D_1 Ansatz with $M = 4$, are compared for the coupling strengths $\alpha = 0.03, 0.1$ and 0.3 . Other parameters are $s = 0.25$, $\Delta/\omega_c = 0.1$, $\epsilon = 0$, $\Lambda = 1.1$ and $N_b = 180$.

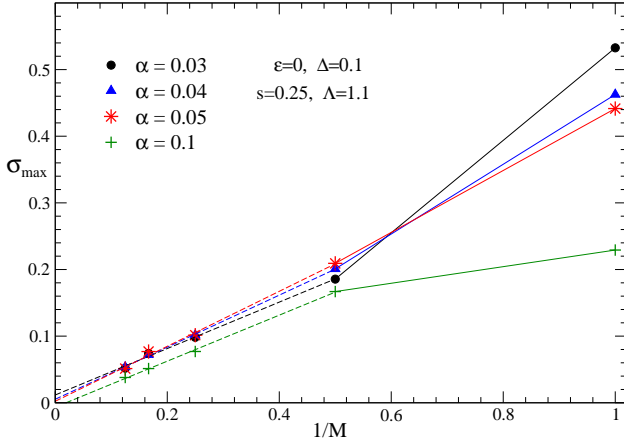


Figure 7: The maximum value of the relative deviation $\sigma_{\max}(M)$ as a function of the multiplicity M of the D_1 Ansatz for the coupling strengths $\alpha = 0.03, 0.04, 0.05$ and 0.1 . An asymptotic value of $\sigma_{\max}(M \rightarrow \infty) \approx 0$ is obtained from the linear fitting (dashed lines). The solid lines are used to connect data points with the same α .

σ_{\max} for $M \rightarrow \infty$, linear fitting

$$\sigma_{\max}(M) = a_1 M^{-1} + a_0 \quad (M > 1), \quad (19)$$

is employed, plotted as dashed lines in Fig. 7. $\sigma_{\max} \rightarrow 0$ linearly with $1/M \rightarrow 0$. The vanishing of $\sigma_{\max}(M)$ indicates that the multi- D_1 Ansatz improves the variational dynamics of the SBM dramatically and may be numerical exact in the weak coupling regime in which the single D_1 Ansatz is known to be inaccurate.

To probe whether the results are reliable for various coupling strengths, the maximum of the relative deviation σ_{\max} is plotted for $M = 1$ and $M = 4$ in Fig. 8 as a function of α . In the weak coupling regime, from $\alpha = 0.01$ to 0.07 , calculated values of σ_{\max} from the sin-

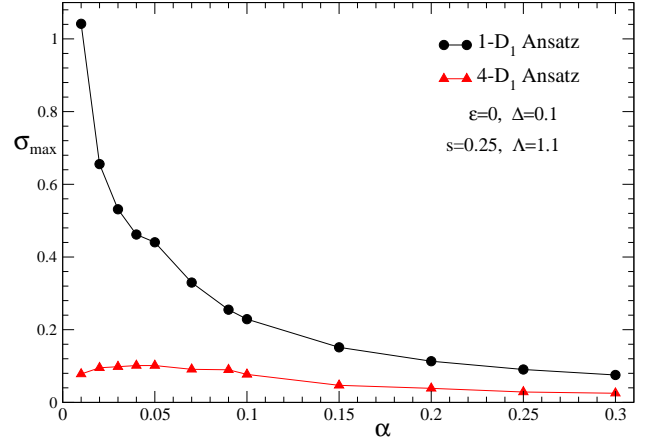


Figure 8: The maximum value of the relative deviation $\sigma_{\max}(\alpha)$ as a function of the coupling strength α of the D_1 Ansatz. The multiplicity $M = 1$ and 4 are plotted. Other parameters $s = 0.25$, $\Delta/\omega_c = 0.1$, $\epsilon = 0$, $\Lambda = 1.1$ and $N_b = 180$.

gle D_1 Ansatz shown as solid dots are larger. In the ultra-weak coupling regime, such as $\alpha \approx 0.01$ and 0.02 , σ_{\max} even exceeds 0.5 , which means that the results are unreliable. The plane-wave like pattern of our results renders the single D_1 Ansatz invalid in this coupling regime. As displayed with solid triangles, results from the multi- D_1 Ansatz have much smaller σ_{\max} than those from the single D_1 Ansatz, indicating that the multi- D_1 Ansatz can capture the plane-wave like pattern more effectively. In the strong coupling regime, the difference in σ_{\max} between the single D_1 and multi- D_1 Ansatz narrows but σ_{\max} for $M = 4$ is still much smaller than that for $M = 1$. It is well known that the single D_1 Ansatz works well in the strong coupling regime [27]. As shown in Fig. 8, the multi- D_1 Ansatz preserves the advantage of the single D_1 Ansatz and performs even better in this regime. It is found that $\sigma_{\max}(\alpha)$ for $M = 4$ is very small for all coupling strengths, thus, it can be concluded that the improved trial wave function can provide a more reliable description of the dynamical behavior of the SBM in the whole parameter regime.

IV. DISCUSSION

In this section we will discuss the dynamical coherent-incoherent crossover. To confirm our method is reliable, results from the multi- D_1 Ansatz are first compared with those from alternative numerical methods. Then simulations are performed to estimate the critical point s_c and sketch the phase diagram.

A. Benchmarking

To confirm that the multi- D_1 Ansatz is reliable under the factorized bath initial condition, we compare

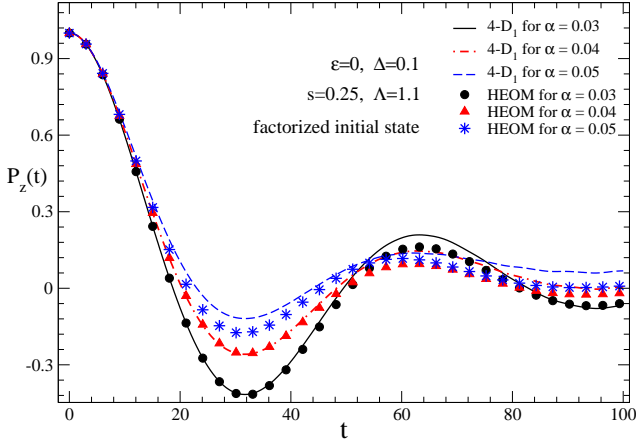


Figure 9: Under the factorized bath initial condition, the population difference $P_z(t)$ calculated by the multi- D_1 Ansatz with $M = 4$ and the extended HEOM method using fitting technique for coupling strengths $\alpha = 0.03, 0.04$ and 0.05 is displayed. Other parameters are $s = 0.25$, $\Delta/\omega_c = 0.1$, $\epsilon = 0$, $\Lambda = 1.1$ and $N_b = 180$.

the population difference $P_z(t)$ from the multi- D_1 Ansatz with that from the HEOM approach [36, 37], as shown in Fig. 9. By fitting the correlation function as a set of exponential functions, we construct the HEOM that can treat dynamics of the SBM at zero temperature (see Appendix B for details). For the weak coupling cases ($\alpha = 0.03$ and 0.04), $P_z(t)$ obtained from the multi- D_1 Ansatz agrees well with that from the HEOM approach. The minor difference in amplitude at longer times may be due to the fact that the upper limit of the integral for the correlation function, $C(t)$ in Eq. (B6), is infinity in the HEOM method, while in the multi- D_1 Ansatz the upper limit of Eqs. (8) and (9) is set to $\omega_{\max} = 4\omega_c$. For a stronger coupling strength, $\alpha = 0.05$, results from these two methods exhibit behaviors of a damped oscillator with the same frequency. However, distinguishable difference in the amplitudes of $P_z(t)$ can be seen. The deviations may be attributed to that at stronger coupling, the HEOM method needs more hierarchy equations to achieve convergence and the exponential fitting of the correlation function in the HEOM method may not be accurate for larger α . In addition, the relative error σ_{\max} at $\alpha = 0.05$ is as small as those at $\alpha = 0.03$ and 0.04 , indicating that the variational dynamics based on the multi- D_1 Ansatz is more accurate than that from the HEOM method at $\alpha = 0.05$.

The polarized initial condition is especially of interest as it corresponds to the typical experimental scenarios [2] in which the system is initialized in the ground state of $\sum_l \omega_l b_l^\dagger b_l + \frac{\sigma_z}{2} \sum_l \lambda_l (b_l^\dagger + b_l) \Big|_{\sigma_z=1}$. To verify the multi- D_1 Ansatz is reliable with the polarized initial bath, the population difference $P_z(t)$ from the multi- D_1 Ansatz is compared with that from the PIMC method [22]. The comparison also checks the reliability of the multi- D_1 Ansatz in a broader parameter space of α . As shown in

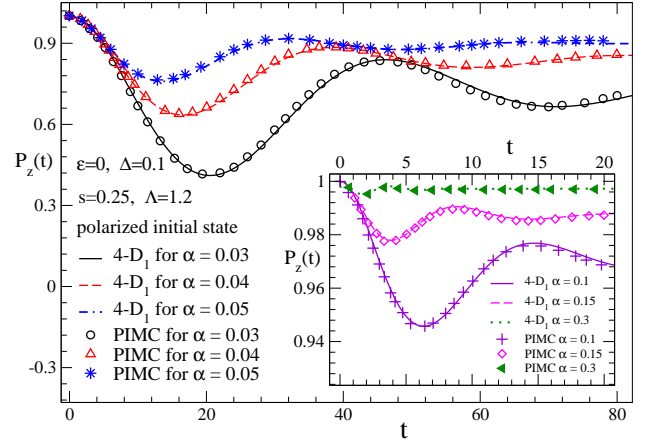


Figure 10: The population difference $P_z(t)$ obtained by the multi- D_1 Ansatz are compared with those calculated by the PIMC method (extracted from Ref.[22]) under the polarized bath initial condition. Other parameters used are $s = 0.25$, $\Delta/\omega_c = 0.1$, $\epsilon = 0$, $\Lambda = 1.2$ and $N_b = 120$.

Fig. 10, for both weak coupling cases of $\alpha = 0.03, 0.04, 0.05$ and strong coupling cases of $\alpha = 0.1, 0.15, 0.3$, the results obtained by the multi- D_1 Ansatz are in excellent agreement with those by the PIMC method. The oscillation frequency turns higher and P_{av} , the average position of $P_z(t)$, approaches 1 with increasing coupling. As pointed out in Sec. IIIB, the initial displacement $-\lambda_l/2\omega_l$ [31] introduces a time-dependent bias $\epsilon(t)$, and $\epsilon(t)$ decays very slowly. Increasing α enlarges $\epsilon(t)$ and moves P_{av} toward 1. Meanwhile, $\epsilon(t)$ also raises the oscillation frequency, and renders more oscillations to appear under the influence of the polarized initial bath.

B. Dynamical crossover

In this subsection, we investigate the dynamical crossovers in the sub-Ohmic SBM. According to Fig. 1(b), in the deep sub-Ohmic regime with s below the critical point s_c , only the coherent phase exists. Above s_c , two lines of the dynamical crossover separate the domain into three parts, and the coherent phase, the incoherent phase and the reemerged coherent phase, occur sequentially with increasing coupling.

To estimate the critical point s_c , simulations are performed for various values of s , corresponding to which dynamic behavior is carefully evaluated. In Figs. 11 and 12, horizontal lines are plotted at the minimum of $P_z(t)$ under various values of α to illustrate whether the dynamics is coherent or incoherent. Shown in Figs. 11(a)-(d) is the population difference $P_z(t)$ at $s = 0.45$ for $\alpha = 0.12, 0.15, 0.23, 0.3$ and 0.5 . A weak oscillation in $P_z(t)$ can be seen in Fig. 11(a) for $\alpha = 0.12$. As demonstrated in Figs. 11(b) and (c), the oscillations of $P_z(t)$ disappear and the system moves to the incoherent phase within the range of $0.15 \leq \alpha < 0.24$. In this param-

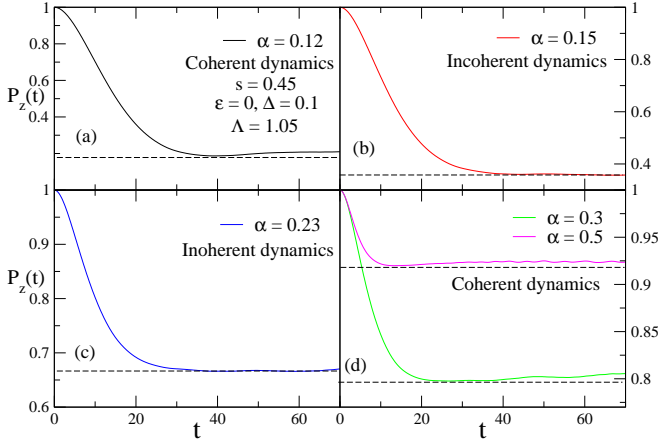


Figure 11: The population difference $P_z(t)$ obtained by the multi-D₁ Ansatz for $s = 0.45$ under the factorized bath initial condition for various coupling strengths α . Other parameters used are $\epsilon = 0$, $\Delta = 0.1$, $\Lambda = 1.05$, and $N_b = 230$. (a) The coherent state occurs at $\alpha = 0.13$. (b)-(c) The incoherent state occurs from $\alpha = 0.15$ to $\alpha = 0.23$. (d) The coherent state recurs at $\alpha = 0.3$. Dashed lines are plotted to show whether the dynamics is coherent or incoherent.

ter region, the oscillation frequency tends to 0, and the damping rate increases with increasing α . The oscillation recurs for $\alpha > 0.24$, as plotted in Fig. 11(d) for $\alpha = 0.3$ and 0.5 . P_{eq} , the steady-state value of $P_z(t)$, approaches 1 and $P_z(t)$ reaches its minimum more rapidly, showing that the oscillation frequency and the damping rate increase with increasing coupling. Contrary to the case of $s = 0.45$, sustained coherence is found for all coupling strengths if $s \leq 0.4$. We perform dynamics simulations at $s = 0.35$ for $\alpha = 0.14, 0.16, 0.18$ and 0.3 to show there is no coherent-to-incoherent crossover for $s \leq 0.4$, which is displayed in Figs. 12(a)-(d). With increasing coupling, both the damping rate and oscillation frequencies increase and only the coherent phase can be seen. The result that the incoherent phase still exists at $s = 0.45$, deviates from the NIBA prediction that there is only the coherent phase for $s < 0.5$. The deviation may be attributed to that the NIBA method is not accurate for systems with long-lasting memory effects [23].

Numerical results are carefully analyzed in the parameter space spanned by s and α in order to arrive at a phase diagram in the vicinity of s_c . Simulations are performed for various coupling strengths α and four bath exponents $s = 0.35, 0.42, 0.45$, and 0.55 . Whether the system is coherent or incoherent, is judged by the existence of population oscillations, which is illustrated through Figs. 11 and 12 with a step size of $\delta\alpha = 0.01$. A sketch of the phase diagram in the vicinity of s_c , is shown in Fig. 13. The shaded incoherent phase domain is bordered by two lines, and with increasing s , the vertical width of the domain expands. Through extrapolation, we estimate $s_c \approx 0.4$. Below s_c , there is no incoherent state, as verified by our simulation for $s = 0.35$. To make the

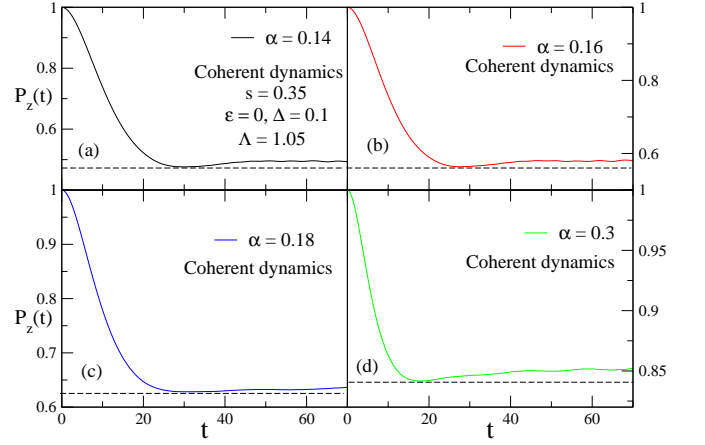


Figure 12: The population difference $P_z(t)$ obtained by the multi-D₁ Ansatz for $s = 0.35$ under the factorized bath initial condition for various coupling strengths α . Other parameters used are $\epsilon = 0$, $\Delta = 0.1$, $\Lambda = 1.05$, and $N_b = 230$. (a)-(d) The coherent state persists at $\alpha = 0.14, 0.16, 0.18$ and 0.3 . Dashed lines are plotted to show the dynamics is coherent.

phase diagram in Fig. 13 comparable with the schematic one shown in Fig. 1(b), we extract data of the localized-delocalized critical line from Ref. [10] and plot it with the black solid line with square symbols. In the scope we plot, the lower coherent-incoherent crossover line is above the phase transition line and their distance decreases with increasing s , which implies that the crossover line and the phase transition line intersect at $s > 0.5$. The phase diagram, shown in Fig. 13, is at variance with that obtained through the NIBA method [22]. From the NIBA method, the coherence does not recur in the strong coupling regime, thus the upper boundary of the shaded area in Fig. 1(b) does not exist in their phase diagram. Meanwhile, the localized-delocalized phase transition line is always below the coherent-incoherent crossover line until they approximately meet at $s = 0.5$. The discrepancy of the two phase diagrams may be due to the approximation used in the NIBA method. In Ref. [22], two cases are analyzed. For case of $s = 0.5$, the authors employ the condition $\alpha \ll \sqrt{\Delta/\omega_c} \approx 0.3$ for $\Delta = 0.1$ and $\omega_c = 1$. While, the upper bound of the incoherent phase for $s = 0.5$, estimated as $\alpha \approx 0.3$ from Fig. 13, is in the area of $\alpha \approx \sqrt{\Delta/\omega_c}$ in which the NIBA method may not give an explicit prediction. For $s \ll 1$, our simulation regime is near $s = 0.5$ where the NIBA method may be only accurate for short times [38]. Though it is difficult to locate the crossover lines accurately from the numerical simulations, it is our hope that the results still convincingly show that the coherence recurs for $s > s_c$ and $s_c \approx 0.4$. Recently, by analyzing the response function, the coherent-incoherent transition point α_{CI} and the critical exponent s_c have been obtained in a slightly different setting [25]. Furthermore, it is pointed out in Ref. [25] that the critical s_c decreases with decreasing Δ/ω_c . The critical exponent obtained in this work should depend on

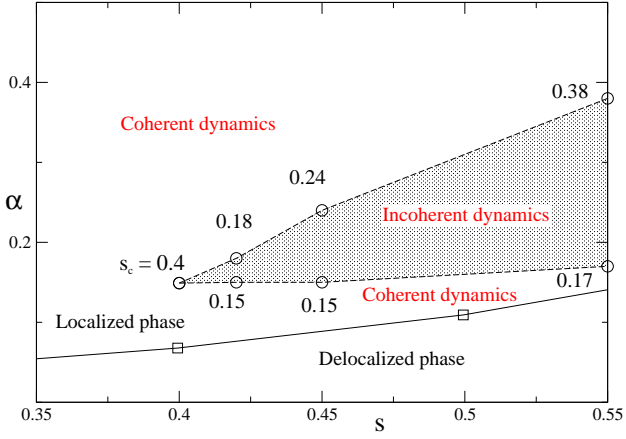


Figure 13: The phase diagram of the dynamical coherent-incoherent crossover near the critical point s_c obtained by the multi- D_1 Ansatz. The critical point $s_c = 0.4$ is estimated by the extrapolation. The domain spanned by s and α is separated by the dashed lines of the coherent-incoherent crossover. The shaded area is the incoherent phase. The solid line with square symbols is the localized-delocalized phase transition line and the data are extracted from Ref. [10].

Δ/ω_c as well, and further simulations need to be carried out to clarify how s_c varies with Δ/ω_c .

To further confirm the picture of the dynamical crossover, $P_z(t)$ is investigated with different initial baths. The system is initialized in the ground state of $\sum_l \omega_l b_l^\dagger b_l + \frac{\sigma_z}{2} \sum_l \lambda_l (b_l^\dagger + b_l) \Big|_{\sigma_z=\mu}$, in which the parameter μ describes the polarization of the initial bath: $\mu = 0$ corresponds to the factorized initial bath, and $\mu = 1$ corresponds to the polarized initial bath. For μ between 0 and 1, the bath is prepared between the two limits. As shown in Fig. 14, $P_z(t)$ at $s = 0.25$ under various values of μ ($\mu = 0, 0.2, 0.4, 0.6, 0.8$ and 1) is plotted. The steady-state value of $P_z(t)$ increases with increasing μ . As shown in the analysis in Sec. III B, the coupling term $\sigma_z/2 \sum_l \lambda_l (b_l^\dagger + b_l)$ in the Hamiltonian of Eq. (1), acts as a time-dependent bias $\epsilon(t)$. As pointed out by Ref. [24], the system is in a quasi-equilibrium state because of $\epsilon(t)$, and $P_z(t)$ appears as a steady-state value due to the ultra-slow dynamics of the sub-Ohmic SBM. Larger μ increases the initial value of $\epsilon(t)$ and yields larger $P_z(t)$. Meanwhile, the frequency of the $P_z(t)$ is also increased because of the time-dependent bias.

V. CONCLUSION

In this work, we have proposed an extended Davydov Ansatz, called the multi- D_1 Ansatz, with a form analogous to the Bloch wave function built from the Davydov D_1 Ansatz (previously known as the delocalized D_1 Ansatz). Dynamics of the sub-Ohmic SBM has been investigated based on the multi- D_1 Ansatz. We perform careful convergence tests for the logarithmic discretiza-

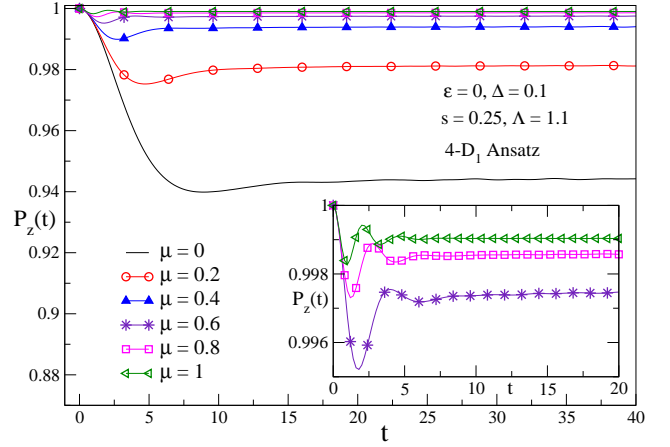


Figure 14: The population difference $P_z(t)$ obtained by the multi- D_1 Ansatz under different initial bath preparation parameters μ , $\mu = 0, 0.2, 0.4, 0.6, 0.8$ and 1. Other parameters used are $s = 0.25$, $\Delta/\omega_c = 0.1$, $\Lambda = 1.1$ and $N_b = 180$.

tion parameter Λ and the frequency lower bound ω_{\min} . To prevent artificial recurrence, a small Λ should be employed. With the same Λ , the dynamics with the factorized initial bath is insensitive to ω_{\min} , yet it is very sensitive with the polarized initial bath. By quantifying how faithfully the Ansatz follows the Schrödinger equation through the relative deviation, we show that the accuracy of the multi- D_1 Ansatz is dramatically improved by increasing the multiplicity M . The dynamical behaviors of the population difference $P_z(t)$ for different coupling strengths and initial bath conditions are studied by the multi- D_1 Ansatz, with results consistent with those from the HEOM and PIMC approaches. It is found that the multi- D_1 Ansatz is a reliable yet unexpectedly efficient method that can treat the coherent and incoherent dynamics in a unified manner.

The coherent-incoherent crossover is also investigated by the multi- D_1 Ansatz. Based on the simulations for various spectral exponents s , the critical point is estimated as $s_c \approx 0.4$, and the phase diagram near s_c is obtained. We find that for $s < s_c$, the coherence will survive for all coupling strengths. Above s_c , the system first goes from the coherent state to the incoherent state with increasing α , and when α increases further, the coherence recurs.

Acknowledgments

The authors thank Vladimir Chernyak and Yiyang Yan for useful discussion. Support from the Singapore National Research Foundation through the Competitive Research Programme (CRP) under Project No. NRF-CRP5-2009-04 is gratefully acknowledged.

Appendix A: The time dependent variational approach for the spin-boson model

In order to apply the Dirac-Frenkel time-dependent variational principle Eq. (4), we first calculate the Lagrangian L by substituting Eq. (3) into Eq. (5),

$$L = \frac{i}{2} \sum_{n=1}^M \sum_{u=1}^M [A_n^* \dot{A}_u - \dot{A}_n^* A_u + \frac{1}{2} A_n^* A_u \sum_k (\dot{f}_{nk} f_{nk}^* + f_{nk} \dot{f}_{nk}^* - \dot{f}_{uk} f_{uk}^* - f_{uk} \dot{f}_{uk}^* + 2f_{nk}^* \dot{f}_{uk} - 2\dot{f}_{nk}^* f_{uk})] R(f_n^*, f_u) + \frac{i}{2} \sum_{n=1}^M \sum_{u=1}^M [B_n^* \dot{B}_u - \dot{B}_n^* B_u + \frac{1}{2} B_n^* B_u \sum_k (\dot{g}_{nk} g_{nk}^* + g_{nk} \dot{g}_{nk}^* - \dot{g}_{uk} g_{uk}^* - g_{uk} \dot{g}_{uk}^* + 2g_{nk}^* \dot{g}_{uk} - 2\dot{g}_{nk}^* g_{uk})] R(g_n^*, g_u) - \langle D(t) | \hat{H} | D(t) \rangle, \quad (\text{A1})$$

where $R(f_n, g_m)$ is the Debye-Waller factor defined in Eq. (11), and the last term in Eq. (A1) with $\epsilon = 0$ can be obtained as

$$\begin{aligned} & \langle D(t) | \hat{H} | D(t) \rangle \\ &= \sum_{n=1}^M \sum_{u=1}^M \left\{ A_n^* A_u \left[\sum_k \omega_k f_{nk}^* f_{uk} + \sum_k \frac{\lambda_k}{2} (f_{nk}^* + f_{uk}) \right] R(f_n^*, f_u) - \frac{\Delta}{2} A_n^* B_u R(f_n^*, g_u) \right. \\ & \quad + B_n^* B_u \left[\sum_k \omega_k g_{nk}^* g_{uk} - \sum_k \frac{\lambda_k}{2} (g_{nk}^* + g_{uk}) \right] R(g_n^*, g_u) \\ & \quad \left. - \frac{\Delta}{2} B_n^* A_u R(g_n^*, f_u) \right\}. \quad (\text{A2}) \end{aligned}$$

Then, Dirac-Frenkel time-dependent variational principle yields the equations of motion for A_n and B_n ,

$$0 = \sum_{m=1}^M \left\{ \left[i\dot{A}_m - \frac{i}{2} A_m \sum_k (\dot{f}_{mk} f_{mk}^* + f_{mk} \dot{f}_{mk}^* - 2f_{nk}^* \dot{f}_{mk}) \right] + A_m \left[\sum_k \omega_k f_{nk}^* f_{mk} + \sum_k \frac{\lambda_k}{2} (f_{nk}^* + f_{mk}) \right] \right\} R(f_n^*, f_m) - \frac{\Delta}{2} \sum_{m=1}^M B_m R(f_n^*, g_m), \quad (\text{A3})$$

and

$$0 = \sum_{m=1}^M \left\{ \left[i\dot{B}_m - \frac{i}{2} B_m \sum_k (\dot{g}_{mk} g_{mk}^* + g_{mk} \dot{g}_{mk}^* - 2g_{nk}^* \dot{g}_{mk}) \right] + B_m \left[\sum_k \omega_k g_{nk}^* g_{mk} - \sum_k \frac{\lambda_k}{2} (g_{nk}^* + g_{mk}) \right] \right\} R(g_n^*, g_m) - \frac{\Delta}{2} \sum_{m=1}^M A_m R(g_n^*, f_m). \quad (\text{A4})$$

And the equations of motion for f_{nl} and g_{nl} are

$$0 = \frac{i}{2} \sum_{m=1}^M \left\{ \left[2\dot{A}_m f_{ml} + 2A_m \dot{f}_{ml} - A_m f_{ml} \sum_k (\dot{f}_{mk}^* f_{mk} + f_{mk}^* \dot{f}_{mk} - 2f_{nk}^* \dot{f}_{mk}) \right] + \omega_l A_m f_{ml} + \frac{\lambda_l}{2} A_m \left[\sum_k \omega_k f_{nk}^* f_{mk} + \sum_k \frac{\lambda_k}{2} (f_{nk}^* + f_{mk}) \right] \right\} R(f_n^*, f_m) - \sum_{m=1}^M \frac{\Delta}{2} B_m g_{ml} R(f_n^*, g_m), \quad (\text{A5})$$

$$0 = \frac{i}{2} \sum_{m=1}^M \left\{ \left[2\dot{B}_m g_{ml} + 2B_m \dot{g}_{ml} - B_m g_{ml} \sum_k (\dot{g}_{mk}^* g_{mk} + g_{mk}^* \dot{g}_{mk} - 2g_{nk}^* \dot{g}_{mk}) \right] + \omega_l B_m g_{ml} - \frac{\lambda_l}{2} B_m \left[\sum_k \omega_k g_{nk}^* g_{mk} - \sum_k \frac{\lambda_k}{2} (g_{nk}^* + g_{mk}) \right] \right\} R(g_n^*, g_m) - \sum_{m=1}^M \frac{\Delta}{2} B_m g_{ml} R(g_n^*, f_m). \quad (\text{A6})$$

Appendix B: Hierarchy equation of motion description of sub-Ohmic spin-boson model

For the spin-boson model Eq. (1), let us denote the eigenstate for the σ_z as σ , then the reduced density matrix element for the two-level system is expressed in the path integral form with the factorized initial condition as [39, 40]

$$\begin{aligned} \rho(\sigma, \sigma'; t) &= \int \mathcal{D}\sigma \int \mathcal{D}\sigma' \rho(\sigma_0, \sigma'_0; t_0) \\ &\times e^{iS[\sigma; t]} F(\sigma, \sigma'; t) e^{-iS[\sigma'; t]}. \quad (\text{B1}) \end{aligned}$$

Here, $S[\sigma]$ is the action of the two-level system, and $F[\sigma, \sigma']$ is the Feynman-Vernon influence functional given by

$$F(\sigma, \sigma'; t) = \exp \left(- \int_0^\infty d\omega J(\omega) \int_{t_0}^t d\tau \int_{t_0}^\tau d\tau' \left[V^\times(\tau) \times \left[V^\times(\tau') \coth \left(\frac{\beta\omega}{2} \right) \cos(\omega(\tau - \tau')) - iV^\circ(\tau') \sin(\omega(\tau - \tau')) \right] \right] \right). \quad (\text{B2})$$

Here we have introduced the abbreviations

$$V = \frac{\sigma_z}{2}, \quad (\text{B3})$$

$$V^\times = V[\tau] - V[\tau'], \quad (\text{B4})$$

$$V^\circ = V[\tau] + V[\tau']. \quad (\text{B5})$$

The correlation function can be written as

$$C(t) = \int_0^\infty d\omega J(\omega) \left[\coth \left(\frac{\beta\omega}{2} \right) \cos(\omega t) - i \sin(\omega t) \right]. \quad (\text{B6})$$

Here, β is the inverse of temperature. If we consider sub-Ohmic spectral density in Eq. (2) and zero temperature case, the correlation function can be easily obtained

$$C(t) = \int_0^\infty d\omega J(\omega) [\cos \omega t - i \sin \omega t] \\ = 2\alpha\omega_c^{1-s} \left\{ \frac{\Gamma(s+1)}{(t^2 + \frac{1}{\omega_c^2})^{\frac{s+1}{2}}} [\cos((s+1) \arctan(\omega_c t)) - i \sin((s+1) \arctan(\omega_c t))] \right\}, \quad (\text{B7})$$

with $\Gamma(x)$ denotes Gamma function. We can further fit the correlation function Eq. (B7) by a set of exponential function as

$$C(t) = \sum_{k=1}^{\text{NA}} a_k e^{-\gamma_k t} - i \sum_{k=1}^{\text{NB}} b_k e^{-\nu_k t}. \quad (\text{B8})$$

Thus, the influence functional Eq. (B2) can be expressed as

$$F(\sigma, \sigma'; t) = \prod_{k=1}^{\text{NA}} \exp \left(- \int_{t_0}^t d\tau \int_{t_0}^\tau d\tau' V^\times(\tau) V^\times(\tau') a_k e^{-\gamma_k(\tau-\tau')} \right) \\ \times \prod_{k=1}^{\text{NB}} \exp \left(- \int_{t_0}^t d\tau \int_{t_0}^\tau d\tau' V^\times(\tau) V^\circ(\tau') - i b_k e^{-\nu_k(\tau-\tau')} \right). \quad (\text{B9})$$

Taking the derivative of Eq. (B1), we have

$$\frac{\partial}{\partial t} \rho(\sigma, \sigma'; t) = -i\mathcal{L}\rho(\sigma, \sigma'; t) - V^\times(t) \int \mathcal{D}\sigma \int \mathcal{D}\sigma' \rho(\sigma_0, \sigma'_0; t_0) \\ \left[\int_{t_0}^t d\tau V^\times(\tau) \sum_{k=1}^{\text{NA}} a_k e^{-\gamma_k(t-\tau)} - i \int_{t_0}^t d\tau V^\circ(\tau) \sum_{k=1}^{\text{NB}} b_k e^{-\nu_k(t-\tau)} \right] \\ \times e^{iS[\sigma; t]} F(\sigma, \sigma'; t) e^{-iS[\sigma'; t]}. \quad (\text{B10})$$

In order to derive the equation of motion, we introduce the auxiliary operator $\rho_{j_1, \dots, j_{\text{NA}}; m_1, \dots, m_{\text{NB}}}(t)$ by its matrix element as [36, 37]

$$\rho_{j_1, \dots, j_{\text{NA}}; m_1, \dots, m_{\text{NB}}}(\sigma, \sigma'; t) = \int \mathcal{D}\sigma \int \mathcal{D}\sigma' \rho(\sigma_0, \sigma'_0; t_0) \prod_{k=1}^{\text{NA}} \left(\int_{t_0}^t d\tau V^\times(\tau) a_k e^{-\gamma_k(t-\tau)} \right)^{j_k} \\ \prod_{k=1}^{\text{NB}} \left(-i \int_{t_0}^t d\tau V^\circ(\tau) b_k e^{-\nu_k(t-\tau)} \right)^{m_k} \\ \times e^{iS[\sigma; t]} F(\sigma, \sigma'; t) e^{-iS[\sigma'; t]}, \quad (\text{B11})$$

for nonnegative integers $j_1, \dots, j_{\text{NA}}; m_1, \dots, m_{\text{NB}}$. Note that only $\rho_{0, \dots, 0}(t) = \hat{\rho}(t)$ has a physical meaning and the others are introduced for computational purposes only. Differentiating $\rho_{j_1, \dots, j_{\text{NA}}; m_1, \dots, m_{\text{NB}}}(\sigma, \sigma'; t)$ with respect to t , we obtain the following hierarchy of equations in operator form

$$\frac{\partial}{\partial t} \hat{\rho}_{j_1, \dots, j_{\text{NA}}; m_1, \dots, m_{\text{NB}}}(t) = - \left[i\mathcal{L} + \sum_{k=1}^{\text{NA}} j_k \gamma_k + \sum_{k=1}^{\text{NB}} m_k \nu_k \right] \hat{\rho}_{j_1, \dots, j_{\text{NA}}; m_1, \dots, m_{\text{NB}}}(t) \\ - V^\times(t) \left[\sum_{k=1}^{\text{NA}} \hat{\rho}_{j_1, \dots, j_k+1, \dots, j_{\text{NA}}; m_1, \dots, m_{\text{NB}}}(t) + \sum_{k=1}^{\text{NB}} \hat{\rho}_{j_1, \dots, j_{\text{NA}}; m_1, \dots, m_k+1, \dots, m_{\text{NB}}}(t) \right] \\ + V^\times(t) \sum_{k=1}^{\text{NA}} j_k a_k \hat{\rho}_{j_1, \dots, j_k-1, \dots, j_{\text{NA}}; m_1, \dots, m_{\text{NB}}}(t) \\ - i V^\circ(t) \sum_{k=1}^{\text{NB}} m_k b_k \hat{\rho}_{j_1, \dots, j_{\text{NA}}; m_1, \dots, m_k-1, \dots, m_{\text{NB}}}(t). \quad (\text{B12})$$

The HEOM consists of an infinite number of equations, but they can be truncated at finite number of hierarchy elements. The infinite hierarchy of Eq. (B12) can be truncated by the terminator as

$$\frac{\partial}{\partial t} \hat{\rho}_{j_1, \dots, j_{\text{NA}}; m_1, \dots, m_{\text{NB}}}(t) = - \left[i\mathcal{L} + \sum_{k=1}^{\text{NA}} j_k \gamma_k + \sum_{k=1}^{\text{NB}} m_k \nu_k \right] \hat{\rho}_{j_1, \dots, j_{\text{NA}}; m_1, \dots, m_{\text{NB}}}(t). \quad (\text{B13})$$

The total number of hierarchy elements can be evaluated as $L_{\text{tot}} = (N_{\text{trun}} + \text{NA} + \text{NB})! / N_{\text{trun}}! (\text{NA} + \text{NB})!$, while the total number of termination elements is $L_{\text{term}} = (N_{\text{trun}} + \text{NA} + \text{NB} - 1)! / (\text{NA} + \text{NB} - 1)! N_{\text{trun}}!$, where N_{trun} is the depth of hierarchy for $m_{q\pm} (q = 1, \dots, N)$. In practice, we can set the termination elements to zero and thus the number of hierarchy elements for calculation can be reduced as $L_{\text{calc}} = L_{\text{tot}} - L_{\text{term}}$.

-
- [1] A. J. Leggett, S. Chakravarty, A. T. Dorsey, M. P. A. Fisher, A. Garg, and W. Zwerger, *Rev. Mod. Phys.* **59**, 1 (1987).
[2] U. Weiss, *Quantum Dissipative Systems*, 3rd ed. (World Scientific, Singapore, 2007).
[3] Y. Yao, L. Duan, Z. Lu, C. Q. Wu, and Y. Zhao, *Phys. Rev. E* **88**, 023303 (2013).

- [4] L. Duan, H. Wang, Q. H. Chen, and Y. Zhao, *J. Chem. Phys.* **139**, 044115 (2013).
[5] Y. Makhlin, G. Schon, and A. Shnirman, *Rev. Mod. Phys.* **73**, 357 (2001).
[6] D. Vion, A. Aassime, A. Cotter, P. Joyez, H. Pothier, C. Urbina, D. Esteve, and M. H. Devoret, *Science* **296**, 886 (2002).

- [7] J. Koch, T. M. Yu, J. Gambetta, A. A. Houck, D. I. Schuster, J. Majer, A. Blais, M. H. Devoret, S. M. Girvin, and R. J. Schoelkopf, *Phys. Rev. A* **76**, 042319 (2007).
- [8] M. Vojta, N. H. Tong, and R. Bulla, *Phys. Rev. Lett.* **94**, 070604 (2005).
- [9] A. Alvermann and H. Fehske, *Phys. Rev. Lett.* **102**, 150601 (2009).
- [10] A. Winter, H. Rieger, M. Vojta, and R. Bulla, *Phys. Rev. Lett.* **102**, 030601 (2009).
- [11] Z. Lv, L. Duan, X. Li, P. Shenai, and Y. Zhao. *J. Chem. Phys.* **139**, 164103 (2013).
- [12] Y. Zhao, Y. Yao, V. Chernyak, and Y. Zhao. *J. Chem. Phys.* **140**, 161105 (2014).
- [13] R. A. Marcus and N. Sutin, *Biochim. Biophys. Acta* **811**, 265 (1985); A. Garg, J. N. Onuchic, and V. Ambegaokar, *J. Chem. Phys.* **83**, 4491 (1985).
- [14] L. Muhlbacher and R. Egger, *J. Chem. Phys.* **118**, 179 (2003); *Chem. Phys.* **296**, 193 (2004).
- [15] R. Bulla, N. H. Tong, and M. Vojta, *Phys. Rev. Lett.* **91**, 170601 (2003); M. Vojta, N. H. Tong, and R. Bulla, *ibid.* **94**, 070604 (2005); F. B. Anders, R. Bulla, and M. Vojta, *ibid.* **98**, 210402 (2007).
- [16] R. Silbey and R. A. Harris, *J. Chem. Phys.* **80**, 2615 (1984).
- [17] A. W. Chin, J. Prior, S. F. Huelga, and M. B. Plenio, *Phys. Rev. Lett.* **107**, 160601 (2011).
- [18] Z. Lv and H. Zheng, *Phys. Rev. B* **75**, 054302 (2007).
- [19] Q. Wang, A. Y. Hu and H. Zheng, *Phys. Rev. B* **80**, 214301 (2009).
- [20] H. Wang and M. Thoss, *New. J. Phys.* **10**, 115005 (2008).
- [21] H. Wang and M. Thoss, *Chem. Phys.* **370**, 78 (2010).
- [22] D. Kast, J. Ankerhold, *Phys. Rev. Lett.* **110**, 010402 (2013).
- [23] D. Kast, J. Ankerhold, *Phys. Rev. B* **87**, 134301 (2013).
- [24] P. Nalbach and M. Thorwart, *Phys. Rev. B* **81**, 054308 (2010).
- [25] P. Nalbach and M. Thorwart, *Phys. Rev. B* **87**, 014116 (2013).
- [26] T. Holstein, *Ann. Phys.* **8**, 325 (1959); **8**, 343 (1959).
- [27] Y. Zhao, D. W. Brown, and K. Lindenberg, *J. Chem. Phys.* **106**, 2728 (1997); **106**, 5622 (1997); **107**, 3159 (1997); **107**, 3179 (1997).
- [28] J. Sun, B. Luo, and Y. Zhao, *Phys. Rev. B* **82**, 014305 (2010).
- [29] J. Ye, K. W. Sun, Y. Zhao, Y. J. Yu, C. K. Lee, and J. S. Cao, *J. Chem. Phys.* **136**, 245104 (2012).
- [30] J. Sun, L. W. Duan, and Y. Zhao, *J. Chem. Phys.* **138**, 174116 (2013).
- [31] N. Wu, L. W. Duan, X. Li, and Y. Zhao. **138**, 084111 (2013).
- [32] N. J. Zhou, L. P. Chen, Y. Zhao, D. Mozyrsky, V. Chernyak, and Y. Zhao. *Phys. Rev. B* **90**, 155135 (2014).
- [33] N. J. Zhou, L. P. Chen, D. Z. Xu, V. Chernyak and Y. Zhao. *Phys. Rev. B* **91**, 195129 (2015).
- [34] T. A. Costi and R. H. McKenzie, *Phys. Rev. A* **68**, 034301 (2003); K. L. Hur, P. D. Beaupre, and W. Hofstetter, *Phys. Rev. Lett.* **99**, 126801 (2007).
- [35] L. Amico *et al.*, *Rev. Mod. Phys.* **80**, 517 (2008).
- [36] A. Ishizaki and Y. Tanimura., *J. Phys. Soc. Jpn.* **74**, 3131 (2005).
- [37] Y. Tanimura, *J. Phys. Soc. Jpn.* **75**, 082001 (2006).
- [38] See Supplemental Material at <http://link.aps.org/supplemental/10.1103/PhysRevLett.110.010402> for details.
- [39] R. P. Feynman and F. L. Vernon, *Ann. Phys. (N.Y.)* **24**, 118 (1963).
- [40] H. Grabert, P. Schramm, and G. L. Ingold, *Phys. Rep.* **168**, 115 (1988).